Scanning Microscopy Vol. 11, 1997 (Pages 81-90) 0891-7035/97$5.00+.25
Scanning Microscopy International, Chicago (AMF O'Hare), IL 60666 USA

PROBE AND OBJECT FUNCTION RECONSTRUCTION IN INCOHERENT SCANNING TRANSMISSION ELECTRON MICROSCOPE IMAGING

P.D. Nellist* and S.J. Pennycook

Oak Ridge National Laboratory, Solid State Division, P.O. Box 2008, Oak Ridge TN 37831-6031

Abstract

Using the phase-object approximation it is shown how an annular dark-field (ADF) detector in a scanning transmission electron microscope (STEM) leads to an image which can be described by an incoherent model. The point spread function is found to be simply the illuminating probe intensity. An important consequence of this is that there is no phase problem in the imaging process, which allows various image processing methods to be applied directly to the image intensity data. Using an image of a GaAs <110>, the probe intensity profile is reconstructed, confirming the existence of a 1.3 Å probe in a 300 kV STEM. It is shown that simply deconvolving this reconstructed probe from the image data does not improve its interpretability because the dominant effects of the imaging process arise simply from the restricted resolution of the microscope. However, use of the reconstructed probe in a maximum entropy reconstruction is demonstrated, which allows information beyond the resolution limit to be restored, and does allow improved image interpretation.

Key Words: Incoherent imaging, scanning transmission electron microscopy, annular dark-field detector, image reconstruction, deconvolution, maximum entropy.

*Address for correspondence:
P.D. Nellist
Nanoscale Physics Research Laboratory,
School of Physics and Astronomy
University of Birmingham
Birmingham B15 2TT, UK
Telephone number: +44-121-4145634
FAX number: +44-121-414-7327
E-mail: P.D.Nellist@bham.ac.uk

Introduction

One of the useful attributes of incoherent imaging is that there is no phase problem. Unlike coherent imaging, in which information is lost at the detection stage by the inability to measure the phase of the image-plane wavefunction, an incoherent image is a convolution between real and positive quantities and therefore there is no phase information to be lost. Lord Rayleigh (1896) has discussed how illuminating a specimen by a large incoherent source renders the specimen effectively self-luminous, and thus the image intensity becomes a convolution between the object function and a point-spread function. By reciprocity (Cowley, 1969; Zeitler and Thomson, 1970) a large detector in a STEM can have a similar effect. Here we use the phase-object approximation to show how an ADF detector leads to incoherent imaging.

It is often the case in transmission electron microscopy (TEM) that an image will consist of a region of interest, such as a crystal defect, surrounded by bulk material of a known structure. The opportunity then arises of using the bulk material to determine the point-spread function applicable to that image, which may then be fed back in to extract more detailed information about the object in the region of interest. Below we discuss how such a reconstruction may be performed experimentally, and then go on to use it for a Wiener deconvolution and a maximum entropy reconstruction as examples of image processing applications.

Incoherent Imaging from Coherent Interference

It has already been shown using the weak phase-object approximation how coherence can be destroyed by an ADF detector (Jesson and Pennycook, 1993). Here we show an alternative approach which demonstrates how the sum in intensity over Bragg scattered beams from a crystalline phase-object leads to incoherent image formation. We start by determining the detector plane intensity. Consider a plane-wave component, with wavevector $\mathbf{k}_i$, within the probe-forming convergent electron beam (Fig. 1). This plane-wave will have a complex amplitude given by the aperture function, $A(\mathbf{k}_i)$.

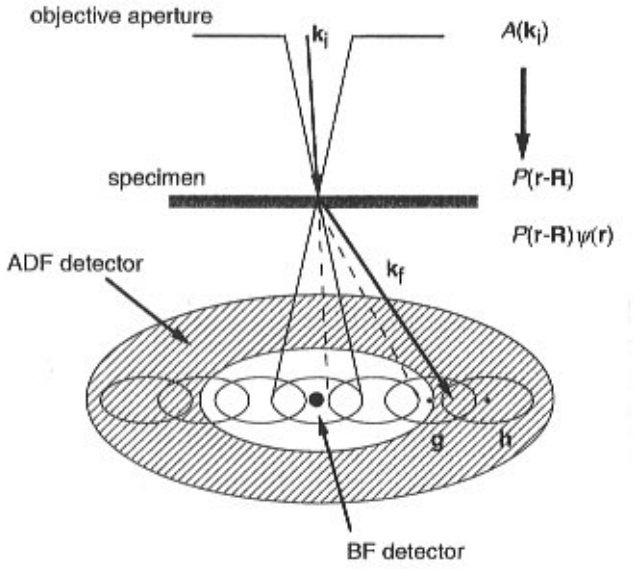

Figure 1. A schematic of the scattering geometry for incoherent image formation from coherently scattered beams. In a STEM, a convergent beam diffraction pattern is formed at the detector plane. Where the diffracted discs overlap, interference can occur resulting in image information. In the case shown above, the bright-field (BF) detector will not be able to resolve the crystal spacing, whereas the annular dark-field (ADF) detector will.

The magnitude of $A(\mathbf{k}_i)$ will be unity for beams within the objective aperture, and zero for those outside; the phase of $A(\mathbf{k}_i)$ is the phase shift produced by the objective lens aberrations, $\chi(\mathbf{k}_i)$, which is given by

$$\chi(\mathbf{k}_i) = \pi\lambda z|\mathbf{k}_i|^2 + 0.5\pi C_s\lambda^3|k_i|^4 \qquad (1)$$

where λ is the electron wavelength, z is the defocus, and C_S is the coefficient of spherical aberration. The amplitude of the electron probe illuminating the specimen, $P(\mathbf{r})$, is then the Fourier transform of the aperture function, $A(\mathbf{k}_i)$, and thus the exit-surface wavefunction is

$$P(\mathbf{r}-\mathbf{R})\,\psi(r) \qquad (2)$$

where $\psi(\mathbf{r})$ is the complex specimen transmission function and $\mathbf{R}$ is the location of the center of the probe. In the phase-object approximation, the specimen transmission function is purely the phase function

$$\psi(\mathbf{r}) = \exp[i\sigma V(\mathbf{r})] \qquad (3)$$

where $V(\mathbf{r})$ is the projected crystal potential, and σ is the interaction constant [see Cowley (1992) for details]. For a perfectly periodic, crystalline specimen, the Fourier transform of Equation (3), denoted $\Psi(\mathbf{k})$, consists of discrete $\ddot{a}$-functions whose magnitudes and phases represent those of the corresponding Bragg beams that would be scattered under conditions of plane-wave illumination.

The propagation of the exit-surface wavefunction to the detector plane can be computed by taking the Fourier transform of Equation (2), so the intensity in the detector plane as a function of scattered wavevector $\mathbf{k}_f$ is

$$M(\mathbf{k}_f,\mathbf{R}) = |[A(\mathbf{k}_f)\exp(i2\pi\mathbf{k}_f\cdot\mathbf{R})]\otimes_{kf}\Psi(\mathbf{k}_f)|^2 \qquad (4)$$

where $\otimes_{kf}$ denotes a convolution with respect to $\mathbf{k}_f$. The product in real-space, Equation (2), forms a convolution in reciprocal space, Equation (4), and the shift in the probe position, $\mathbf{R}$, leads to the aperture function being multiplied by a linear phase function across reciprocal-space. The observed intensity in the detector plane is therefore a series of discs, each centered on the position of where the Bragg spot would be observed in the case of axial plane-wave illumination. Since the probe-position, defocus, and aberration information is carried by the phase in each disc, image contrast can only be observed if the discs overlap (Spence and Cowley, 1978), as illustrated in Figure 1.

To understand the properties of the disc-overlap region, consider the overlap between discs from the diffracted Bragg beams $\mathbf{g}$ and $\mathbf{h}$ (Fig. 1), with the complex amplitude, $\Psi(\mathbf{k})$, of the Bragg beams at $\mathbf{g}$ and $\mathbf{h}$ denoted by Ψ_g and Ψ_h respectively. Within this overlap, the detector plane intensity, $M(\mathbf{k}_f, \mathbf{R})$, can be written

$$\begin{aligned} M(\mathbf{k}_f,\mathbf{R}) = {} & |\Psi_g|^2 + |\Psi_h|^2 \\ & +2|\Psi_g||\Psi_h|\cos[2\pi\mathbf{R}\cdot(\mathbf{h}-\mathbf{g})+(\chi(\mathbf{k}_f-\mathbf{g})-\chi(\mathbf{k}_f-\mathbf{h})) \\ & +(\angle\Psi_g-\angle\Psi_h)] \end{aligned} \qquad (5)$$

with the phase of Ψ_g written as $\angle\Psi_g$, and re-writing $A(\mathbf{k})$ as the pure phase $\exp(i\chi(\mathbf{k}))$. The imaging information is all carried by the cosine interference term, the argument of which itself contains three distinct terms. The first term of the cosine argument shows that the intensity in all points in the overlap region oscillates with respect to the probe movement, at a spatial frequency given by the reciprocal lattice vector joining the Bragg spots, $(\mathbf{h}-\mathbf{g})$. This implies that for many Bragg beams being detected, the contribution to the image at a spatial frequency, $\boldsymbol{\rho}$, is only from the disc overlap regions between Bragg beams separated by the two-dimensional vector, $\boldsymbol{\rho}$. The second term in the cosine argument of Equation (5) contains the effects of defocus and the lens aberrations. The phase of the intensity oscillation just mentioned is modified by the difference in the phase of the two overlapping aperture functions. What is observed is therefore a series of fringes in the overlap

region [see for example, Nellist *et al*. (1995)], whose form is determined by defocus and the lens aberrations, and which appear to travel as the probe is scanned. The final phase term in the cosine argument of Equation (5) is the phase difference between the diffracted beams in question, and it is this term that carries the structural information regarding the specimen to the detector plane. In general, Rodenburg and Bates (1992) have shown that the Fourier transform of $M(\mathbf{k}_f,\mathbf{R})$ with respect to $\mathbf{R}$ is given by a convolution between two overlapping aperture functions and the interference term between parts of the scattering function separated by ρ, thus

$$G(\mathbf{k}_f,\boldsymbol{\rho}) = [A(\mathbf{k}_f - \boldsymbol{\rho}/2)A^*(\mathbf{k}_f+\boldsymbol{\rho}/2)]\otimes_{kf}[\boldsymbol{\Psi}(\mathbf{k}_f+\boldsymbol{\rho}/2)\boldsymbol{\Psi}^*(\mathbf{k}_f-\boldsymbol{\rho}/2)] \quad (6)$$

We are now in a position to compare the coherent and incoherent imaging modes. We simply integrate Equation (6) over the relevant detector function $D(\mathbf{k}_f)$, which results in the Fourier transform of the detected image intensity,

$$i(\boldsymbol{\rho}) = \int D(\mathbf{k}_f) \int A(\mathbf{k}_i\ \boldsymbol{\rho}/2)A^*(\mathbf{k}_i+\boldsymbol{\rho}/2)\Psi(\mathbf{k}_f\ \mathbf{k}_i+\boldsymbol{\rho}/2) \Psi^*(\mathbf{k}_f\ \mathbf{k}_i\ \boldsymbol{\rho}/2)d\mathbf{k}_i\, d\mathbf{k}_f \quad (7)$$

where we have now written out the convolution in Equation (6) in full, using $\mathbf{k}_i$ as the dummy variable since the convolution arises physically from the cone of incident wavevectors forming the probe, and the scattering is done by the specimen from $\mathbf{k}_i$ to $\mathbf{k}_f$.

Coherent imaging requires the use of a detector which is significantly smaller than the objective aperture radius, such as a small axial detector for bright-field (BF) imaging (Fig. 1), which is equivalent to nearly plane-wave illumination in a conventional transmission electron microscope (CTEM) by reciprocity. The detector will typically be smaller than the fringe features in the disc overlaps, and therefore the image intensity will be strongly dependent on both the position of the detector and the phase of the aperture function, as is well known in phase-contrast microscopy. In general, the image contrast is not likely to be a direct structure image of the object.

In contrast, incoherent imaging uses a detector which is significantly *larger* than the objective aperture radius, such as the annular dark-field (ADF) detector in Figure 1, which is equivalent to using a large incoherent source in conventional imaging as suggested for the light-optical analogue situation by Lord Rayleigh (1896). The Fourier component of an ADF image at the spatial frequency $\boldsymbol{\rho}$ can now be seen to be arising from the interference between the many pairs of Bragg discs that are separated by $\boldsymbol{\rho}$. Mathematically we note that if the geometry of $D(\mathbf{k}_f)$ is large compared to the aperture function, we can neglect overlaps that are intersected by the edges of the detector allowing the integrals in Equation (7) to be separated to form

$$i(\boldsymbol{\rho}) = \int A(\mathbf{k}_i\ \boldsymbol{\rho}/2)A^*(\mathbf{k}_i+\boldsymbol{\rho}/2)d\mathbf{k}_i \int D(\mathbf{k}_f)\Psi(\mathbf{k}_f+\boldsymbol{\rho}/2) \Psi^*(\mathbf{k}_f-\boldsymbol{\rho}/2)d\mathbf{k}_f \quad (8)$$

The $\boldsymbol{\rho}$ Fourier component is therefore the product between a transfer function, $T(\boldsymbol{\rho})$, which is given by the integral in intensity over the fringes in one disc overlap, and an object spectrum, $W(\boldsymbol{\rho})$, which is given by the sum of the scattering interference terms that give rise to the interference observed by the annular detector. The transfer function, $T(\boldsymbol{\rho})$, is thus the integral over the phase difference between two overlapping aperture functions separated by $\boldsymbol{\rho}$,

$$T(\boldsymbol{\rho}) = \int A(\mathbf{k}_f)A^*(\mathbf{k}_f+\boldsymbol{\rho})d\mathbf{k}_f \quad (9)$$

which is identical to the autocorrelation function of $A(\mathbf{k})$. The Fourier transform of the autocorrelation of $A(\mathbf{k})$ is $|P(\mathbf{r})|^2$, the probe *intensity* function, thus the ADF image intensity in real-space becomes

$$I(\mathbf{R}) = |P(\mathbf{R})|^2\otimes_R O(\mathbf{R}) \quad (10)$$

a convolution between the probe intensity and an object function, and is the definition of an incoherent image. A coherent image cannot be written in this form because the range of the integral over $\mathbf{k}_f$ in Equation (7) is restricted so that the Ψ terms are also dependent on $\mathbf{k}_i$.

An important advantage of incoherent imaging over coherent imaging is that the resolution is doubled. Since the transfer, $T(\boldsymbol{\rho})$, is the autocorrelation of $A(\mathbf{k})$, it has twice the width in reciprocal space than $A(\mathbf{k})$, which can be expressed in real-space by stating that the intensity of the probe is narrower than the magnitude of $P(\mathbf{r})$. It can also be seen in Figure 1 that the spacing leading to the diffracted discs shown will not be resolvable in the BF image, because the detector is not in an overlap region, whereas the ADF detector will be receiving an interference signal and thus the spacing will be resolved.

The object spectrum, $O(\mathbf{r})$, is the Fourier transform of $W(\boldsymbol{\rho})$, which itself can be written

$$W(\boldsymbol{\rho}) = \int D_{ADF}(\mathbf{k}_f)\Psi(\mathbf{k}_f + \boldsymbol{\rho}/2)\Psi^*(\mathbf{k}_f - \boldsymbol{\rho}/2)d\mathbf{k}_f \quad (11)$$

where $D_{ADF}(\mathbf{k}_f)$ is the detector function and has a value of unity for final wavevectors detected, zero otherwise. Taking the Fourier transform of Equation (11) can be shown to give

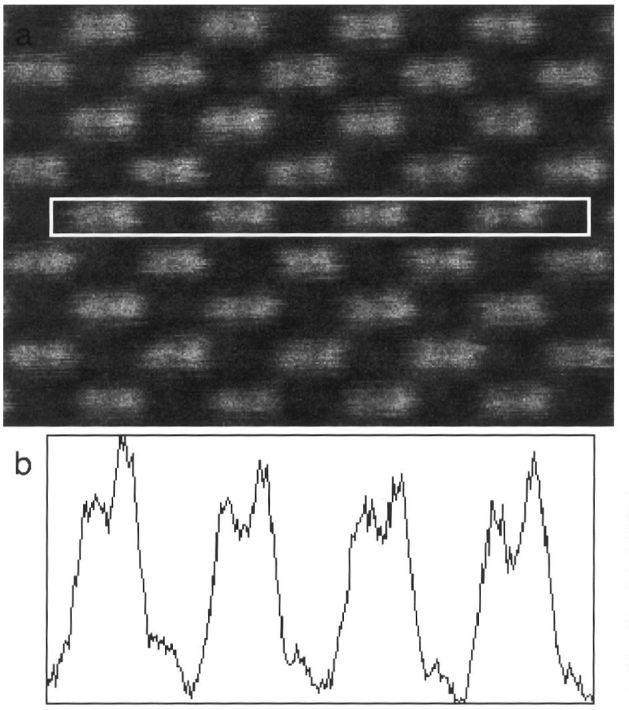

Figure 2. (**a**) Raw image of GaAs <110>. The intensity profile along the area indicated, with intensities summed across the width, is shown in (**b**). The 1.4 Å "dumbbell" spacing is resolved, and the polarity of the lattice is obvious with the As columns forming the right-hand side of each dumbbell.

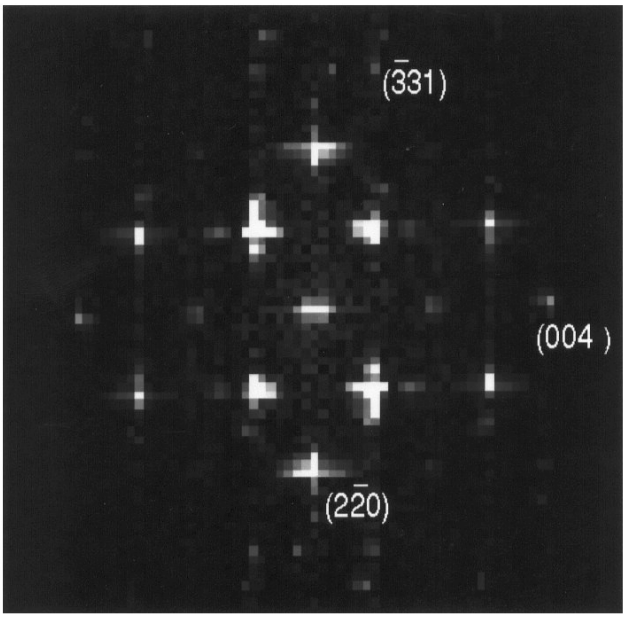

Figure 3. The magnitude of the Fourier transform of the image shown in Figure 2a. The spots out as far as (004), which is the dumbbell spacing, can be clearly seen. There is some evidence of the {331} spots, but these are very close to the noise level.

$$O(\mathbf{R}) = \int \Psi(\mathbf{R}+\mathbf{c}/2)\psi^*(\mathbf{R}-\mathbf{c}/2)s(\mathbf{c})d\mathbf{c} \qquad (12)$$

the ADF object function. Equation (12) is a real-space integral over a coherence envelope, $s(\mathbf{c})$, which is the Fourier transform of the detector function; $\mathbf{c}$ is the dummy variable of integration. In the case of an infinite detector $s(\mathbf{c})$ is a δ-function, and $O(\mathbf{r})$ becomes simply $|\psi(\mathbf{R})|^2$, which is perfect incoherence. For a phase object, however, this condition also implies no contrast since $|\psi(\mathbf{R})|^2$ is unity everywhere, which is expected since we are detecting all transmitted electrons and the phase-object has no absorption. In order to see some phase-contrast we require a finite coherence envelope, which physically means that we require some interference within the scattered wave. Substituting Equation (3) into Equation (12), and assuming an ADF detector, but neglecting the outer radius which experimentally is usually much larger than any significant electron scattering, gives

$$O(\mathbf{R}) = 1 - \int h(\mathbf{c}) \cos\{\sigma[V(\mathbf{R}+\mathbf{c}/2)-V(\mathbf{R}-\mathbf{c}/2)]\}\, d\mathbf{c} \qquad (13)$$

where $h(\mathbf{c})$ is the Fourier transform of the function describing the hole in the detector, and using the centrosymmetry of $h(\mathbf{c})$. Thus it can now be seen that the object function is related to the slope of the object potential within the coherence envelope. As long as the width of the coherence envelope is smaller than the projected interatomic spacing, which can be achieved by making the inner radius sufficiently large, then each atomic column will act as an independent scatterer, and $O(\mathbf{R})$ will be a map of atomic columns. Since the strength of $O(\mathbf{R})$ is dependent on the slope of the potential, the image will show a sensitivity to atomic number, hence the name Z-contrast.

Of course Equation (13) will become more difficult to interpret as the coherence envelope becomes comparable to interatomic spacings, or as the phase argument of the cosine function starts to become large. Although the phase-object is useful for illustrating how an incoherent image can be formed, we should perhaps not worry too greatly about its quantitative behavior because it does not take account of the propagation through the thickness of the specimen. However, the approach taken above can be extended to give a coherence envelope in dynamical scattering (Nellist and Pennycook, 1999), but the algebra is somewhat more complicated. It is found that the geometry of the ADF detector is not so efficient at destroying coherence along each atom column, so although the transverse incoherent model of Equation (10) still holds, the object function may

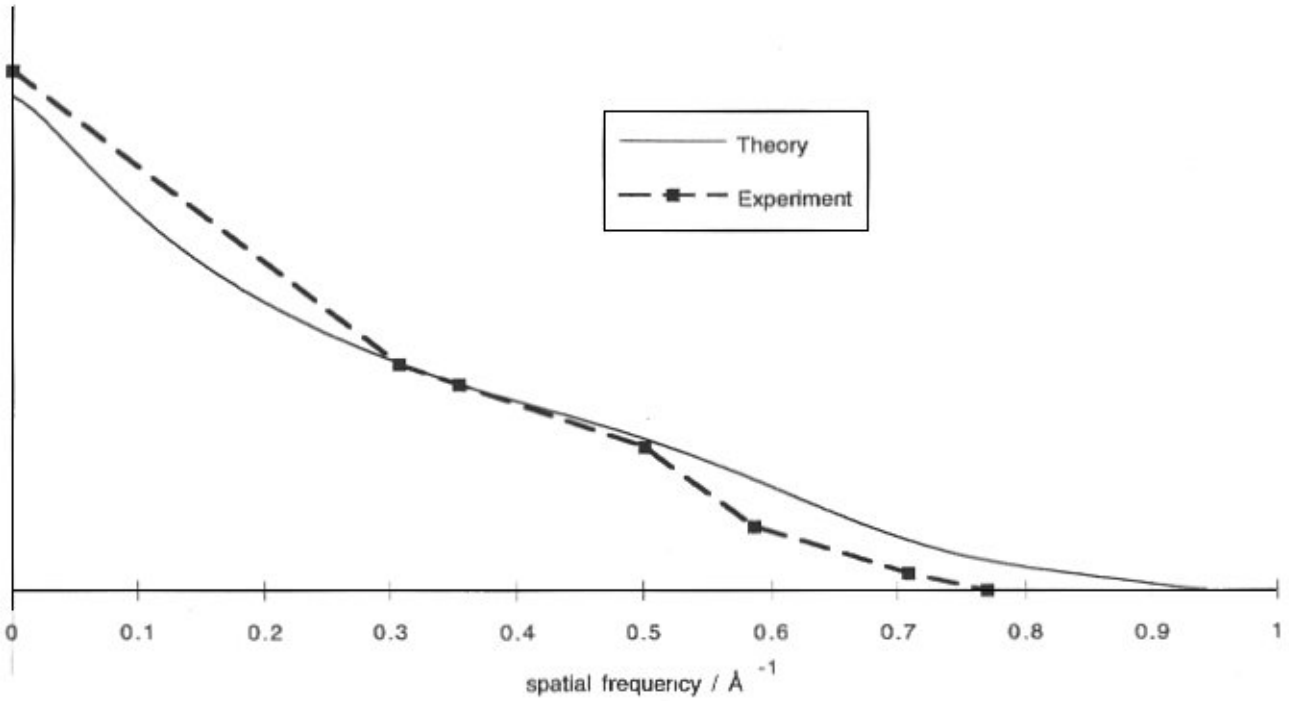

Figure 4. The transfer function reconstructed from the experimental data compared to the theoretical optimum transfer for the HB603U microscope (300 kV, *C*S =1 mm) as function of spatial frequency. In the experimental case, the data points are reconstructed from the image data, and a linear interpolation is constructed between them.

show a non-linear thickness dependence (see for example Jesson and Pennycook, 1993). However, the phase-object approach taken above demonstrates the principles of how incoherent phase-contrast can be achieved, and we now proceed to examine how image processing methods may be applied to incoherent TEM imaging.

Experimental Probe Function Reconstruction

In practical applications of TEM, the image often consists of a localized region of interest, such as a crystal defect, surrounded by relatively large regions of bulk crystalline material. Since the structure of the bulk material is usually known, it is possible to use these regions of the image to determine some imaging parameters. A much more rigorous interpretation of the detail in the area of interest then becomes possible.

Since for incoherent imaging the image intensity itself is the convolution between a real-positive object function and a real-positive probe function, if we know the object function for the bulk crystalline material, then it should be possible to solve for the probe function. Unfortunately, there are two main problems with this scheme. First, a region of perfect crystal carries relatively little information. The image can be expressed by a few discrete Fourier components, and even if we knew the object function exactly, we would still only be able to determine the transfer function at the spatial frequencies represented in the image. Second, the exact form of the object function may not be straightforward to compute from the known structure because this also requires, amongst other things, an exact knowledge of the degree of partial coherence remaining in the scattering. The effects of these concerns are best illustrated with an example.

A raw image of GaAs viewed along the <110> direction is shown in Figure 2a. This image was taken in a VG Microscopes (East Grinstead, UK) HB603U STEM (300 kV C_S = 1 mm) using an ADF detector with an inner radius of 30 mrad. As expected, the image is a direct or *structure* image of this material, with the "dumbbell" structure well resolved. The intensity profile in Figure 2b shows how the polarity of the crystal structure is directly represented in the image. The magnitude of the Fourier transform of this image (Fig. 3) shows spots out as far the {004} spacings (0.14 nm), and there is weak evidence of the {331} spacings (0.13 nm). We proceed by assuming that the object function is an array of δ-functions weighted by the Z^2 of the atomic species of the column, from which the object function Fourier component magnitudes can be calculated. Dividing the experimental Fourier component magnitudes by those

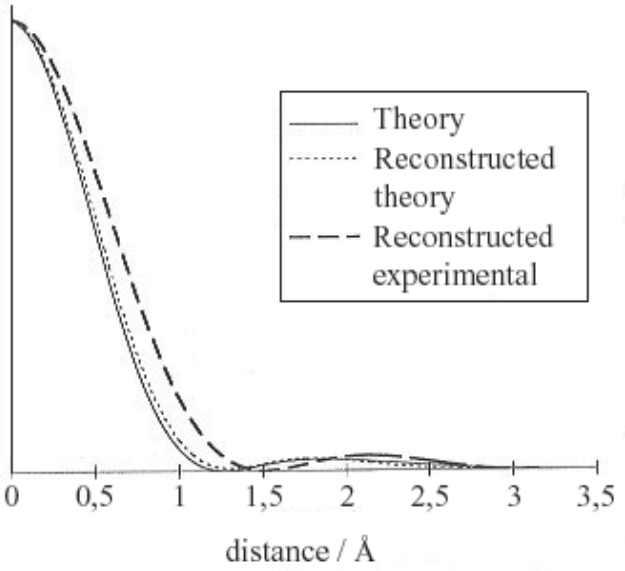

Figure 5. The probe intensity reconstructed from the experimental data compared to the theoretical optimum probe for the HB603U, plotted as a function of radius. To check the validity of using a linear interpolation between data points in reciprocal space, a reconstructed probe is also shown by using the theoretical optimum transfer values, but only at the spatial frequencies used for the experimental reconstruction. The only effect is a very slight broadening of the probe profile.

calculated for the object function results in an estimate of the transfer function at each Fourier component. Circular symmetry is assumed, allowing us to deal with a one-dimensional radial transfer function. Where we have more that one spot with the same magnitude of spatial frequency we have simply taken the mean value, though a more sophisticated approach could use variations in the transfer between these spots to determine non circular symmetric components in the probe, such as astigmatism. To reconstruct the probe we need a continuous transfer function over reciprocal space, which is now achieved by simply performing a linear interpolation between the points (see Fig. 4). This procedure is justified because the transfer function is typically a slowly varying function, and the corners introduced by a linear interpolation will lead to some weak intensity at large distances in real-space, which are neglected. The fine structure in the probe, which is the crucial part for high-resolution detail in the image, is controlled by the slowly varying trends in the transfer function, which are reasonably well retained using a linear interpolation. Finally, the probe is reconstructed by performing an inverse zero-order Fourier-Bessel transform (also known as a Hankel transform). Figure 5 shows the reconstructed probe compared to the optimum theoretical probe for the HB603U. Also shown is a probe reconstructed using calculated optimum transfer values, but at only the Fourier components found in GaAs, to test the functioning of the linear interpolation which has broadened the probe profile only very slightly.

The probe reconstructed from experimental data has a full width at half maximum (FWHM) of 1.3 Å, demonstrating the performance of the microscope, though this can be seen to be a little larger than the width of the optimum theoretical probe. The approximation of the object function to δ-functions is unlikely to be valid, and the width of the atomic column object function will broaden the reconstructed probe. However, the broadening of the reconstructed probe is only about 0.3 Å, and thus is very much smaller than the interatomic spacings involved in this image. It is more difficult to judge the effects of partial coherence in the object function, though the fact that the reconstruction has a reasonable form is supportive of the incoherent model. Fourier transforms of images of Si<110> have shown a weak (002) spot (Hillyard and Silcox, 1995), however, which is forbidden if the columns are perfectly incoherent. The calculated transfer at the (002) frequency would therefore be infinite, with catastrophic consequences on the probe reconstruction. In the GaAs reconstruction presented here, however, the transfer calculated from the (002) spot was reasonable, supporting the model of perfect incoherence in this case.

Object Function Reconstruction

Having determined the probe function for a given image, we should now consider how it can be used to gain further object information from that image. One of the major advantages of incoherent imaging is that the images can be directly inverted to the projected atomic structure, because the peaks in intensity are located over the atomic columns. Image simulations from trial structures are not required. A typical probe, however, has weak subsidiary maxima adjacent to the primary maximum (Fig. 5), which can lead to weak artifacts in the image, as shown by the profile in Figure 2. These artifacts are extremely weak compared to the main peaks, and are usually not a source of confusion. In principle, though, we should now be able to account for them, and be able to sharpen the image somewhat, using the reconstructed probe profile.

First, we note that the transfer function falls to zero at about 1.1 Å, thus imposing an information limit. Any magnitude in the Fourier transform of the image intensity beyond this information limit has been introduced by the image forming process, such as because of quantum noise. A low-pass filter is thus extremely useful for removing this unwanted, high-spatial frequency information from the image. The first-order Butterworth filter has the form

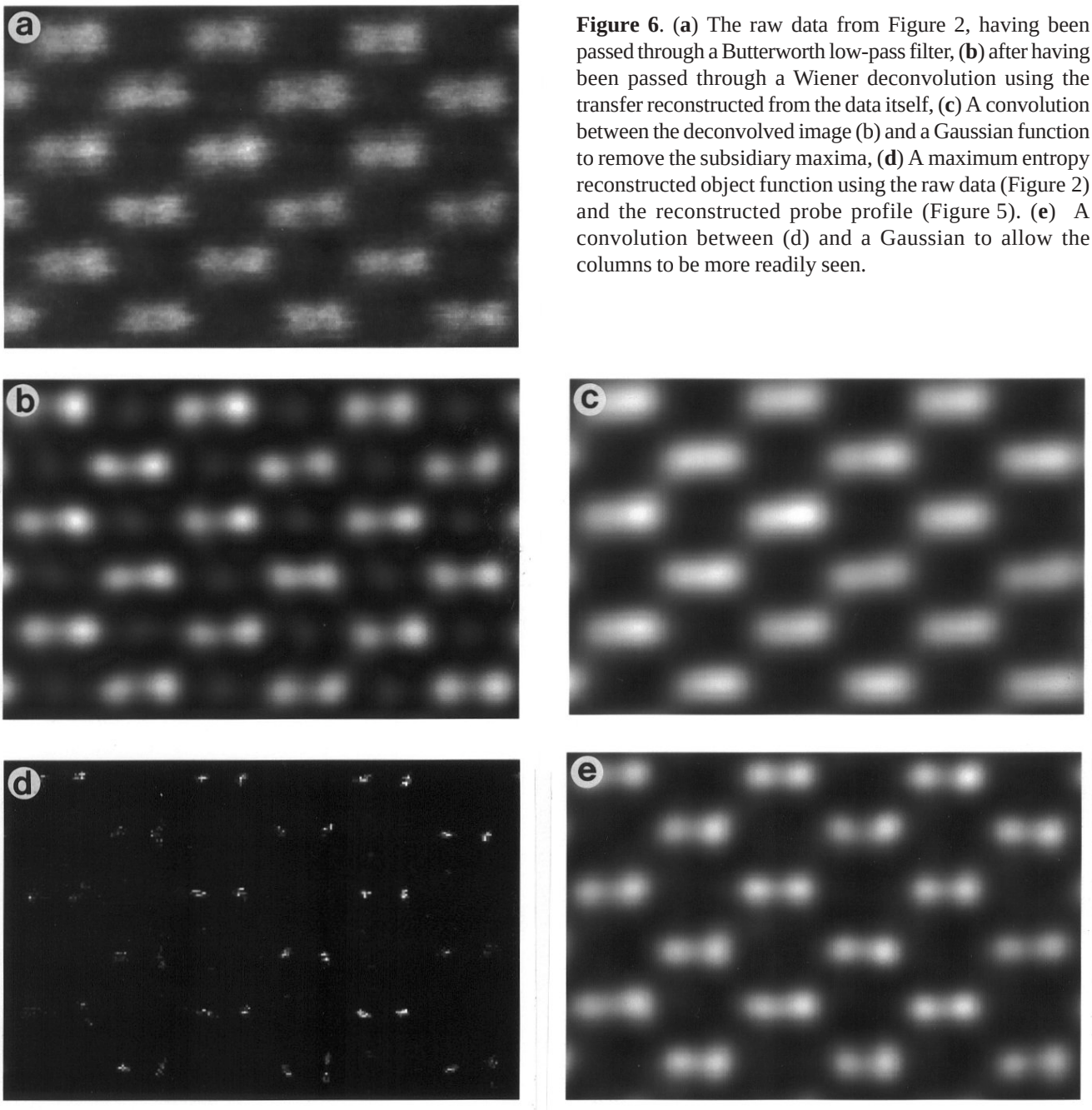

Figure 6. (**a**) The raw data from Figure 2, having been passed through a Butterworth low-pass filter, (**b**) after having been passed through a Wiener deconvolution using the transfer reconstructed from the data itself, (**c**) A convolution between the deconvolved image (b) and a Gaussian function to remove the subsidiary maxima, (**d**) A maximum entropy reconstructed object function using the raw data (Figure 2) and the reconstructed probe profile (Figure 5). (**e**) A convolution between (d) and a Gaussian to allow the columns to be more readily seen.

$$F(\rho) = \frac{1}{1+(\rho/\rho_0)^2} \tag{14}$$

as a function of spatial frequency ρ, where ρ_0 is a constant controlling the width of the filter. It does not lead to the addition of further artifacts (Fig. 6a), and the simple smoothing action performed by this filter has removed much of the quantum noise.

Since we know the probe profile, the next thing to try is a deconvolution. The effect of multiplying the image Fourier transform by the Wiener filter

$$F(\rho) = \frac{T^*(\rho)}{|T(\rho)|^2 + \varepsilon} \tag{15}$$

results in Figure 6b [see Bates and McDonnell (1986) for details of the application of Wiener filters]. Although the effects of the noise have been suppressed and the atoms in the dumbbells are now well resolved, the tail artifacts in the image have been enhanced. The explanation of this effect also explains the origin of the tails. The probe tails arise because the Fourier transform of the probe is truncated in

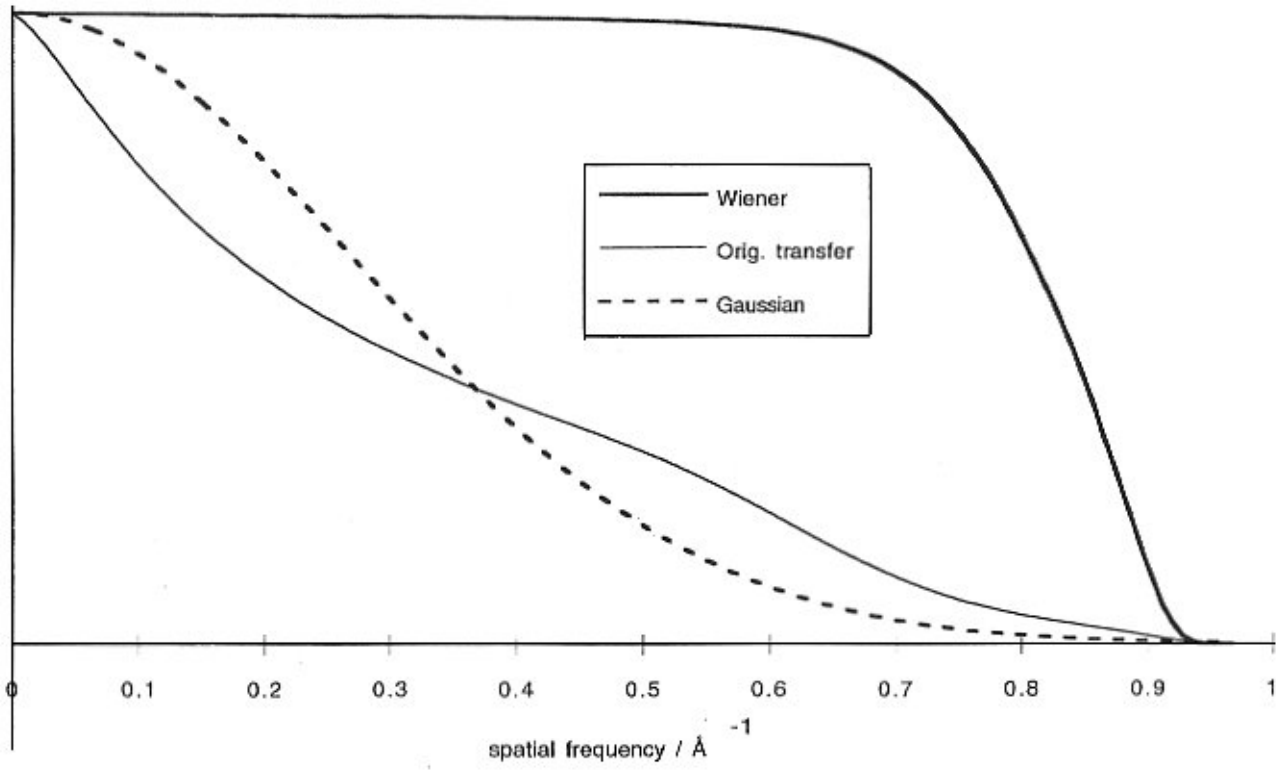

Figure 7. The resulting transfer functions after Wiener filtering, then subsequent reconvolution with a gaussian, compared to the optimum theoretical transfer. Note how the Wiener filter leads to a more strongly truncated transfer function.

reciprocal space. A function that is localized in reciprocal space must be somewhat delocalised in real space. A tail-less point spread function, such as a Gaussian, has a longer, asymptotically decaying tail extending over all reciprocal space. A Wiener filter acts by dividing out the transfer function resulting in a constant transfer. However, a constant, ε, is required to decay the resulting transfer to zero where $T(\rho)$ becomes small at the information limit. The resulting transfer (Fig. 7) is even more strongly truncated in reciprocal space, leading to the enhanced tail artifacts which make the image even harder to directly interpret. The only way to remove the tails is to have a slowly decaying transfer that becomes negligible at the information limit, such as the gaussian shown in Figure 7, but this is in effect simply reversing the effects of the original deconvolution. Using a gaussian re-convolution to remove the tails results in Figure 6c, in which the high spatial frequencies have now been suppressed to such an extent that the dumbbells are now hardly resolved. This example illustrates how the probe tails are a result of the resolution limit of the microscope, which imposes the Fourier space truncation, and demonstrates how imaging near the resolution limit of an optical instrument can cause complications. The solution is to retrieve information from beyond the information limit, which either requires a higher resolution microscope, or using a constraint to enable a mathematical reconstruction of the object function.

Iterative deconvolution methods allow the inclusion of constraints. Here we show the use of the maximum entropy image reconstruction technique developed by Gull and Skilling (1984). The algorithm used here takes the experimental image and a point spread function as inputs, and thus assumes incoherent imaging. The point spread function is simply the probe intensity function. As an example we have reconstructed the GaAs image in Figure 2a, with the probe profile reconstructed from it (Fig. 5). The resulting reconstructed object function (Fig. 6d) shows major peaks in intensity at the atom sites, with most of the dumbbell spacings within 0.1 Å of the correct value . The narrow width of the peaks shows that the object function has now been reconstructed beyond the information limit. The variation of the width, and splitting, of some of the peaks can be attributed to microscope instabilities blurring some parts of the image, and these widths can therefore be used as a measure of the uncertainty in the atom column locations. The reconstructed object also shows some

weaker structure that has been introduced by the noise in the experimental data. It is at this point that the microscopist applies their skill and experience to interpret the data, for instance deciding whether a split feature is actually separate atoms that were unresolved in the original image, or whether the feature is due to noise or instabilities and the splitting just represents an uncertainty in the actual column position. To help make this distinction, the reconstructed object function from the known bulk crystalline region of the image can be used to determine the expected uncertainty for a single column. Having done this, for visualization purposes it is useful to re-convolve the object function with a gaussian so that the split peaks that are assigned to a single column become a single, slightly elongated feature (Fig. 6e). This reconstructed image has achieved a sharpening of the column features, with the dumbbells more strongly resolved, without the accompanying strengthening of the inter-column artifacts.

Conclusions

Using the phase-object approximation, we have demonstrated that using an annular dark-field detector in a STEM, with a sufficiently large inner radius, leads to incoherent imaging. The phase-object approximation assumes perfectly coherent scattering, and therefore it is purely the large geometry of the detector that breaks the coherence. Intrinsically incoherent scattering processes within the specimen act to supplement this coherence breaking action (Jesson and Pennycook, 1996), but are not necessary for incoherent imaging. For instance, the incoherent integration over transverse phonon modes for phonon scattering has the same effect as the integration over final wavevectors for the large detector. However, it was shown that phonon modes with wavevectors parallel to the beam direction can destroy coherence along a column of atoms much more efficiently than an annular detector.

One of the useful attributes of incoherent imaging is that there is no phase problem since the image intensity is simply a convolution between a real-positive object function and a real-positive point-spread function. Thus image processing techniques can be applied directly to such images. Where the image is of a known material, it can be used to determine the probe function acting on the image. Although it should be noted that an image of a perfect crystal does not contain complete information on the probe profile, a good estimate of it can be made. A direct deconvolution of the probe function does not add to the interpretability of the image data because artifacts in the image from the probe profile are due to the resolution limit, beyond which there is no information passed by the microscope.

Image processing techniques can play a role if they can reconstruct the object function beyond the information limit. Some kind of constraint is required to do this, and we have demonstrated the use of maximum entropy which allows more detailed information to be retrieved from the image. The maximum entropy constraint is that of maximum object function likelihood in the absence of any further experimental evidence. A more sophisticated reconstruction scheme might use further constraints such as atomicity or minimum inter-column spacings. We should stress in conclusion, though, that the majority of ADF images can be directly interpreted from the raw image data, perhaps with a simple low-pass filter applied to remove some of the noise.

Acknowledgements

This work was performed at Oak Ridge National Laboratory, managed by Lockheed Martin Energy Research Corp. for the U.S. Department of Energy under contract number DE-AC05-96OR22464, and through an appointment to the Oak Ridge National Laboratory Postdoctoral Program administered by ORISE.

References

Bates RHT, McDonnell MJ (1986) Image Restoration and Reconstruction. Oxford Engineering Science Series No. 16. Oxford University Press, Oxford. pp 76-78.

Cowley JM (1969) Image contrast in a transmission scanning electron microscope. Appl Phys Lett **15**: 58-59.

Cowley JM (1992) Electron Diffraction: An Introduction. In: Electron Diffraction Techniques Vol. 1. Cowley JM (ed). Oxford University Press, Oxford. pp 1-74.

Gull SF, Skilling J (1984) Maximum entropy methods in image processing. IEE Proc **131F**: 646-659.

Hillyard S, Silcox J (1995) Detector geometry, thermal diffuse scattering and strain effects in ADF STEM imaging, Ultramicroscopy **58**: 6-17.

Jesson DE, Pennycook SJ (1993) Incoherent imaging of thin specimens using coherently scattered electrons. Proc Roy Soc Lond **A441**: 261-281.

Jesson DE, Pennycook SJ (1995) Incoherent imaging of crystals using thermally scattered electrons. Proc Roy Soc Lond **A449**: 273-293.

Nellist PD, Pennycook SJ (1999) Incoherent imaging using dynamically scattered electrons. Ultramicroscopy **78**: 111-124.

Nellist PD, McCallum BC, Rodenburg JM (1995) Resolution beyond the information limit in transmission electron microscopy. Nature **374**: 630-632.

Rayleigh Lord (1896) On the theory of optical images with special reference to the microscope. Phil Mag **42**: 167-195.

Rodenburg JM, Bates RHT (1992) The theory of

super-resolution electron microscopy via Wigner-distribution deconvolution. Phil Trans R Soc London A **339**: 521-553.

Spence JCH, Cowley JM (1978) Lattice imaging in STEM. Optik **50**: 129-142.

Zeitler E, Thomson MGR (1970) Scanning transmission electron microscopy. Optik **31**: 258-280 and 359-366.